Nanoscale

COMMUNICATION

View Article Online
View Journal | View Issue

Cite this: *Nanoscale*, 2025, **17**, 12094

Received 28th January 2025,
Accepted 14th April 2025

DOI: 10.1039/d5nr00419e

rsc.li/nanoscale

NiFeMo layered triple hydroxide and MXene heterostructure for boosted oxygen evolution reaction in anion exchange membrane water electrolysis†

Santanu Pal,[a,c] Ekta Chaturvedi,[a,c] Chandni Das,[a,c] Nibedita Sinha,[a,c] Tanbir Ahmed[a,c] and Poulomi Roy *[a,b,c]

Efficient, low cost and stable electrocatalysts are highly desirable for overcoming the sluggish kinetics of the oxygen evolution reaction (OER) in alkaline water electrolysis for hydrogen production. Interfacial engineering of heterostructures is quite beneficial for improving charge transfer efficiency at the interface. In this context, heterostructures of layered triple hydroxides (LTHs) and MXenes have shown great potential as OER electrocatalysts owing to their 2D–2D structure and unique physiochemical properties. Coupling LTHs with MXenes can potentially enhance their conductivity and stability, thereby boosting OER activity. In this study, we report a heterointerface between NiFeMo-LTH on $Ti_3C_2T_x$ MXene, which exhibited superior catalytic activity and stability in alkaline freshwater and seawater, reducing the activation energy. Importantly, the heterostructure achieved a current density of 100 mA cm^{-2} at the cost of 292 mV and 340 mV overpotentials in alkaline saline water and real seawater, respectively, and showed robustness over 100 h without hypochlorite formation in alkaline real seawater, exhibiting corrosion-resistant behaviour. Moreover, NiFeMo-LTH/MXene explored in alkaline anion exchange membrane water electrolyzer (AEMWE) achieved a current density of 750 mA cm^{-2} at 2.16 V cell voltage at an operating temperature of 60 °C with an energy efficiency of 60.5%. Raman analysis and XPS analysis post stability test demonstrated easy electron transfer from LTH to MXene at the heterointerface, leading to the formation of NiOOH electroactive species that facilitated the OER activity.

1. Introduction

Clean and green energy production using renewable energy resources is one of the best ways to address global energy demand and avoid environmental pollution.[1,2] In this context, hydrogen can fulfil global future energy demands owing to its high combustion energy and net zero emission technology.[3,4] Electrochemically driven water splitting involving anodic oxygen evolution reaction (OER) and cathodic hydrogen evolution reaction (HER) can be considered a sustainable and efficient way to produce clean hydrogen.[5,6] Recently, anion exchange membrane water electrolysis (AEMWE) has emerged as a cost-effective, eco-friendly and sustainable technology for industry level production of hydrogen, consuming a large volume of water.[7,8] Although AEMWE is anticipated as one of the most needed technology, scarcity of water in future will surely hinder its wide application. Considering seawater as the most abundant water resource, direct seawater splitting, especially in offshore, may be realized as an indispensable technique to be adapted.[9,10]

However, for the extensive use of seawater, there are challenges in terms of performance and sustainability owing to the severe corrosion at the anode caused by different interfering elements, especially chlorides.[11–13] The approach of interfacial solar desalination, converting seawater into hot vapour followed by vapour splitting, could be an effective alternative to direct seawater electrolysis or photocatalysis. However, the approach needs improved efficiencies, device design optimization and stability to make the process efficient and competitive.[14,15] To achieve effective and sustainable seawater splitting, the development of an OER-active electrocatalyst with a corrosion resistance property is highly desirable.[16,17] Thermodynamically, alkaline seawater electrolysis is preferred over acidic medium with limiting overpotential of 480 mV to avoid chloride electrochemistry, known as the chlorine evolution reaction (CER).

[a]*CSIR – Central Mechanical Engineering Research Institute (CMERI), Mahatma Gandhi Avenue, Durgapur 713209, West Bengal, India*
[b]*Physical & Materials Chemistry Division, CSIR – National Chemical Laboratory (NCL), Dr Homi Bhabha Road, Pune 411008, India*
[c]*Academy of Scientific and Innovative Research (AcSIR), Ghaziabad, Uttar Pradesh, 201002, India. E-mail: poulomiroy@yahoo.com*

† Electronic supplementary information (ESI) available. See DOI: https://doi.org/10.1039/d5nr00419e

Transition metal-based layered double hydroxides with the general formula $[M_{1-x}^{2+}M_x^{3+}(OH)_2]^{x+}(A^{n-})_{x/n}$ (where M is a bimetallic or trimetallic metal and A is an intercalated ions) have been the primary choice for researchers in this regard owing to their 2D lamellar structure, tuneable interlayer spacing, chemical compositions and large active surface area.[18,19] The anticorrosive nature of LDHs owing to their anionic species in the interlayer spacing shows their potential for direct seawater splitting.[20,21] Most commonly, NiFe-LDH has been explored as OER-active electrocatalyst in alkaline freshwater as well as seawater electrolyte medium.[22,23] However, the performance of bimetallic LDH encounters limitations due to poor ionic conductivity and inadequate availability of active sites.[12,24] Our group explored different strategies, including three or more element incorporation in LDH, resulting in enhanced interlayer spacing between adjacent layers, and the incorporation of anionic guest species to boost the activity and to attain stability in alkaline seawater.[18–21] The drawbacks of LDHs can also be overcome by combining with other 2D materials with better conductivity, mechanical strength and stability as a heterostructure. Although graphenes are well known in this regard, their hydrophobicity may not be supportable for this application. Instead, MXene is a new 2D material with remarkable physiochemical properties including high electrical conductivity, super hydrophilicity with modifiable terminal groups is a more suitable candidate to produce a heterostructure with LDH.[25] MXene has the general formulae of $M_{n+1}X_nT_x$ (n = 1, 2, or 3), where M, X, and T represent the transition metal, C and N, and surface functional groups (–OH, –O, and –F) which are generally synthesized from the MAX phase by selective etching and stripping.[26] The coupling of LDH and MXene as a heterostructure offers favourable electronic charge distribution at the interface, increasing the electrocatalytic activity.[27] While dealing with seawater, MXene has the advantage of acting as a corrosion inhibitor by blocking the diffusion of corrosive ions like chlorides, providing much needed protection to the electrode during seawater electrolysis.[28]

Most reports on LDH/MXene hybrid materials were explored in freshwater. For instance, Yu *et al.* reported NiFe-LDH/Ti_3C_2-MXene where NiFe LDH was electrochemically deposited on MXene coated nickel foam (NF) and showed excellent OER activity, achieving a current density of 500 mA cm^{-2} with an overpotential of 300 mV.[29] The synergistic coupling between LDH and MXene layers and strong electronic interaction accelerated ionic transport and rapid gas evolution from the electrode with good stability. Chen *et al.* reported hypophosphite intercalated FeNi LDH combined with V_2C MXene in which lowering of the d band centre preferentially decreased the ΔG value, thereby promoting the OER process.[30] Hu *et al.* synthesized MOF derived CoFe LDH/Ti_3C_2 MXene with good OER activity and the binding strength of the oxygenated intermediate was modulated during the OER.[31] Yan and co-workers incorporated the O-vacancy in FeNi-LDH by Cr doping and the synergy between the O-vacancy and MXene led to a good OER overpotential of 232 mV at 10 mA cm^{-2}.[32]

These results indicate that an LDH and MXene combination can potentially achieve high OER activity, although direct seawater splitting remains unexplored. Herein, we developed NiFeMo layered triple hydroxide (LTH), which showed high OER activity by introducing Mo as the third metal species and further combined with Ti_3C_2 MXene forming the NiFeMo-LTH/Ti_3C_2 MXene heterostructure. The heterostructure boosts the OER activity and retards chloride to attain longer stability in alkaline seawater media. We further explored the performance of the heterostructure in the AEMWE set up to understand the potential of the developed electrocatalyst towards practical applications for hydrogen production.

2. Experimental section

2.1 Chemicals

Titanium aluminium carbide powder (Ti_3AlC_2) of highly pure (99%, Sigma-Aldrich) MAX phase was used for MXene preparation. Nickel(II) chloride hexahydrate ($NiCl_2{\cdot}4H_2O$), iron chloride ($FeCl_3$, anhydrous), sodium molybdate dihydrate ($Na_2MoO_4{\cdot}2H_2O$), urea, commercial RuO_2 and Pt/C, potassium hydroxide (KOH), sodium chloride (NaCl), ethanol (C_2H_5OH), lithium fluoride (LiF) and hydrochloric acid (HCl) were purchased from Sigma-Aldrich. Nickel foam was purchased from MTI corporation, KJ group. All the reagents and chemicals are A.R grade and used without further purification.

2.2 Materials synthesis

2.2.1 Synthesis of $Ti_3C_2T_x$ MXene nanosheets. MXene was prepared using Ti_3AlC_2 MAX phase through the mild etching method using LiF/HCl. Initially, 1 g of Ti_3AlC_2 MAX phase was added into LiF/HCl etchant solution at 40 °C at a stirring rate of 400 rpm for 48 h. After 48 hours, the solution was mixed with distilled water and centrifuged at 2500 rpm for 5 min followed by collection of MXene sediment. The cycle was repeated 8–10 times until the pH of the supernatant reached 6. Later, this dark supernatant was carefully vacuum filtered to collect MXene powder which was dried and used for further experiments.

2.2.2 Synthesis of NiFeMo-LTH/$Ti_3C_2T_x$ MXene and NiFeMo-LTH. Typically, a simple hydrothermal method was adopted to synthesize NiFeMo-LTH and NiFeMo-LTH/MXene heterostructure. The hydrothermal technique was chosen over other techniques, like sol–gel or electrochemical deposition for several reasons. First, the hydrothermal process promotes homogeneous nucleation and growth of LTH nanoflakes on MXene, leading to strong coupling effects and better bonding between LTH and MXene. Secondly, the morphology of LDH can be easily tuned by the hydrothermal method. Thirdly, the hydrothermal method provides better crystallinity and increased surface area which leads to improved electrochemical activity.

To synthesize NiFeMo-LTH/MXene, 10 mM $NiCl_2{\cdot}4H_2O$, 5 mM $FeCl_3$, 5 mM $Na_2MoO_4{\cdot}2H_2O$, 0.1 M urea and 0.05 M NH_4F were dissolved in 25 mL ultra-pure water and the solu-

tion was stirred for 30 min (solution A). In another container 10 mg of MXene powder was dispersed in 10 mL of urea aqueous solution in an Ar atmosphere (solution B). Solution A was added to solution B and stirred vigorously for 15 min. The homogeneous mixture was then transferred in a Teflon-lined autoclave, sealed and maintained at 120 °C for 12 h in a hot air oven. After the completion of the reaction, the autoclave was allowed to cool naturally, and the product was collected *via* centrifugation, washed several times with distilled water and ethanol, and dried under vacuum at 60 °C overnight. The as-obtained product was labelled as NFM-LTH/MXene.

For the synthesis of NFM-LTH, the same procedure was followed as discussed above without adding solution B containing MXene suspension. The reaction parameters were tabulated in Table S1.†

2.3 Characterization of materials

Powder X-ray diffraction (XRD) patterns were collected using a Rigaku Miniflex 600 XRD diffractometer (40 kV, 15 mA) with a Cu k_α radiation of wavelength 1.54 Å. The morphology of the as prepared samples was characterized by SEM analysis with the help of field emission scanning electron microscopy (FE-SEM, Carl Zeiss, Germany) operating at 5 kV. The elemental composition with atomic% of the materials were evaluated using an energy dispersive X-ray spectrometer (EDS) associated with the FE-SEM instrument. In depth microstructural properties of the samples were obtained through high resolution transmission electron microscopy (HRTEM) (FEI TECNAI 20 G2, Netherlands, 200 kV). The TEM specimen was prepared by dispersing a small amount of powder sample into pure ethanol and a drop of homogeneous solution was casted on the carbon coated Cu grid and dried. The surface composition and valence states of the samples were determined using X-ray photoelectron spectroscopy (XPS) recorded using a SCIENTA R-3000 analyser with a monochromatic Al Ka source. A 2×10^{-10} torr vacuum ambit chamber was maintained during XPS analysis. The instrument was calibrated before use with Au and Ag foils. Charge neutralization was used for all measurements using a combination of low-energy Ar^+ ions and electrons, and the charging effects were compensated by shifting binding energies based on the adventitious C 1s peak (284.8 eV). Raman spectra of the prepared samples was acquired using an alpha300 RAS (WITec Instruments) Raman spectrometer.

2.4 Electrode preparation and electrochemical measurements

All electrochemical experiments were performed in a Metrohm Autolab 204 at room temperature using 1 M KOH (pH = 13.9) as electrolyte with a standard three electrode configuration. The as prepared catalyst on Ni foam, saturated Hg/HgO, and Pt wire were used as the working electrode, reference electrode and counter electrode, respectively in three electrode configurations. The working electrode was prepared by drop casting the electrocatalyst ink on Ni foam. The ink was prepared by ultrasonicating 4 mg of the catalyst in a mixture of 600 μL deionized water, 300 μL isopropanol and 100 μL of polyvinylidene difluoride (PVDF) solution for 30 min to form a homogenous suspension. Prior to drop-casting, bare Ni foams were etched using 3 M HCl solution to remove the native oxide layer, followed by washing with DI water and ethanol. The mass loading of the electrocatalysts on the treated Ni foam was maintained between 0.8–1 mg cm^{-2}. Commercial RuO_2 on Ni foam and bare nickel foam (NF) was used as a reference with a mass loading of 0.5 mg cm^2 for the comparative electrochemical study. To avoid the effect of NF, we also drop casted the catalyst ink on a glassy carbon electrode (GCE) and checked the performances. The electrochemical studies were carried out in 1 M KOH containing deionized water to evaluate the inherent electrochemical properties of electrocatalysts. Further, the electrocatalytic activities of the developed heterostructure was explored in highly saline alkaline water containing 1 M KOH + 1 M NaCl, 1 M KOH + 0.5 M NaCl, alkaline (1 M KOH) simulated seawater and real seawater. The simulated seawater was prepared by mixing 26.73 g of NaCl, 2.26 g of $MgCl_2$, 3.25 g of $MgSO_4$, 1.12 g of $CaCl_2$, 0.19 g of $NaHCO_3$, 3.48 g of Na_2SO_4 and 0.72 g of KCl in 1 L of ultrapure water. The real seawater was collected from the Bay of Bengal, Digha, West Bengal, India (21.62°45′27″N, 87.53°01′67″E).

To activate the electrode materials before data collection for OER measurements, all working electrodes were pre-activated *via* cyclic voltammetry (CV) scanning at 40 mV s^{-1} in 1 M KOH electrolyte. Polarization curves were obtained using linear sweep voltammetry (LSV) at a scan rate of 2.0 mV s^{-1}. The LSV curves were represented with 90% *iR* compensation to avoid uncompensated series resistance of the electrochemical circuit (R_s). All the measured potentials were converted into a reversible hydrogen electrode (RHE) and calibrated with 90% *iR* compensation using eqn (1) and (2):

$$E_{RHE} = E_{apply} + E_{Hg/HgO} + (0.059 \times pH) \quad (1)$$

$$E_{iR} = E_{RHE} - iR_s \quad (2)$$

The overpotential (η) and Tafel slope (b) of water oxidation were calculated using eqn (3) and (4):

$$\eta = E_{RHE} - 1.23 \quad (3)$$

$$\eta = a + b \log j \quad (4)$$

The activation energy (E_a) was determined using polarization curves of OER between 30 to 60 °C. Electrochemical impedance spectroscopy (EIS) curves were obtained throughout a frequency range of 100 kHz to 0.1 Hz with an amplitude of 5 mV. Cyclic voltammograms with varied scan rates (40–200 mV s^{-1}) in the 0.96–1.0 V *vs.* RHE region were used to determine the double layer capacitance (C_{dl}) of the catalysts. The value of C_{dl} was calculated by taking half of the difference between the anodic and cathodic current density against the scanning rate. The electrochemical

active surface area (ECSA) was derived from C_{dl} values through eqn (5):

$$\text{ECSA} = \frac{C_{dl}}{C_s} \quad (5)$$

where C_s is the specific charge resistance of the working electrode which has the value of 40 μF cm^{-2} in alkaline solutions. Mass activity (j_{mass}) was calculated using eqn (6):

$$\text{Mass activity (MA)} = \frac{j}{m} \quad (6)$$

A long-term stability test was evaluated using a chronoamperometry method for 100 h at current densities of 100 and 500 mA cm^{-2}, respectively.

2.5 Turn over frequency (TOF)

TOF was determined based on the number of total active sites for all electrodes using the following given eqn (7):

$$\text{TOF} = \frac{j \times A}{\alpha \times F \times n} \quad (7)$$

where j (A cm^{-2}) is the current density at a particular overpotential, A (cm^2) is the geometric surface area of the working electrode, F is the Faraday constant (96 485 C mol^{-1}), α is the number of electron transfers and $n = Q_s/F$ is the number of active sites during the electrochemical reaction process. Here, surface charge (Q_s) is calculated from integrated area of the redox peak of the CV plot.

2.6 Corrosion study

Corrosion studies of NFM-LTH/MXene, NFM-LTH and bare nickel foam (NF) were performed in 1 M KOH + 1 M NaCl electrolyte in three electrode configurations. The sample electrodes were immersed in electrolyte solution for 1 h to reach a stable open circuit potential (OCP). The electrochemical impedance spectroscopy (EIS) measurements were carried out at an OCP between 100 kHz to 0.01 Hz with an amplitude of 5 mV. The corrosion characteristics were further analyzed using the Nyquist plots. The Tafel test was carried out in the potential range from −0.4 to 0.2 V *vs.* the Hg/HgO reference electrode (the potential range was chosen based on the OCP). The corrosion potential (E_{corr}) and corrosion current (I_{corr}) were measured from the Tafel analysis of the polarization curve.

2.7 Iodometry test

To check whether any hypochlorite (ClO^-) was generated, iodometry tests were conducted using 10 mL of electrolyte solution after long term stability test in 1 M KOH + seawater electrolyte. At first, the electrolyte solution was acidified (pH = 2) by adding the required volume of 0.5 M H_2SO_4 solution. Then, 5 mL of freshly prepared KI solution was added to the solution. ClO^- formation was ignored since no yellow colouration was observed in the solution sample.

2.8 Electrolyzer assembly and experiment setup

The electrolyzer cell was assembled with current collectors, two PTFE gaskets, cathode and anode substrates, Sustainion® X37-50 grade RT membrane as anion exchange membrane (AEM) and a continuous flow design on the anode and cathode sides. NFM-LTH/MXene catalyst ink was spray coated on Ni foam for its use as an anode and Pt/C containing ink was spray coated on Ni foam for use as a cathode for anion exchange membrane water electrolysis (AEMWE). Prior to spray coating, the 2.6 × 2.6 cm^2 Ni foams were cleaned with 3 M HCl to remove the native oxide layer followed by washing with DI water and ethanol. The catalyst ink was prepared by dispersing 40 mg of catalyst powder in 4 mL of water-isopropanol mixture and 100 μL of PVDF (1 wt%) solution as binder by ultrasonication. Then, the spray coated catalyst ink on Ni foams were dried in vacuum and a mass loading of 1.5 mg cm^{-2} and 1 mg cm^{-2} was maintained for the anode and cathode, respectively. For comparison, RuO_2 loaded NF was prepared as an anode using the same process with a mass loading of 1 mg cm^{-2}. The 1 M KOH was used as catholyte and anolyte and was circulated by two single channel peristaltic pumps using a flow rate of 50 mL min^{-1}. Initially, the anode and cathode materials were placed in the accurate position of flow plates, separated using AEM and then an equal compression torque was applied to complete the MEA process.

All electrolyzer tests were performed on the same workstation (Metrohm Autolab M204) with a 10 A current booster. LSVs were collected at an operating temperature of 60 °C with a scan rate of 50 mV s^{-1}. The chronopotentiometry test was conducted at 60 °C at a current density of 100 and 200 mA cm^{-2} under electrolyte flow conditions in the electrolyzer.

2.9 Calculation of AEM electrolyzer energy efficiency, energy consumption and H_2 cost

The electrolyzer energy efficiency was calculated based on the method described in earlier studies.[33,34]

i. H_2 production rate at 0.5 A cm^{-2}:

$$= (j \text{ A cm}^{-2})\ (1\ e^-/1.602 \times 10^{-19}\ \text{C})\ (1\ H_2/2\ e^-)$$

$$= 0.5 \text{ A cm}^{-2}/(1.602 \times 10^{-19}\ \text{C} \times 2)$$

$$= 2.59 \times 10^{-6} \text{ mol } H_2 \text{ per cm}^2 \text{ per s}$$

ii. LHV of H_2:

$$= 120 \text{ MJ kg}^{-1}\ H_2$$

$$= 2.42 \times 10^5 \text{ J mol}^{-1}\ H_2$$

iii. H_2 power out:

$$= (2.59 \times 10^{-6} \text{ mol } H_2 \text{ per cm}^2 \text{ per s}) \times (2.42 \times 10^5 \text{ J mol}^{-1}\ H_2)$$

$$= 0.627 \text{ W cm}^{-2}$$

iv. Electrolyzer power at 0.5 A cm^{-2}:

$$= 0.5\ \text{A cm}^{-2} \times 2.07\ \text{V}$$

$$= 1.035\ \text{W cm}^{-2}$$

v. Electrolyzer efficiency:

$$= (\text{H}_2\ \text{power out})/(\text{electrolyzer power})$$

$$= 0.627\ \text{W cm}^{-2}/1.035\ \text{W cm}^{-2} = 60.5\%$$

vi. Energy consumption of per gasoline-gallon equivalent (GGE) H_2

$$= 1\ \text{GGE H}_2/(\text{H}_2\ \text{production rate}) \times \text{electrolyzer power}$$

$$= 0.997\ \text{kg}/(2.59 \times 10^{-6}\ \text{mol H}_2\ \text{per cm}^2\ \text{per s} \times 2\ \text{kg mol}^{-1}) \times 1.035\ \text{W cm}^{-2}$$

$$= 55.5\ \text{kW h}$$

vii. Price per gasoline-gallon equivalent (GGE) H_2

$$= \frac{1\text{GGE H}_2 \times \text{electrolyzer power} \times \text{electricity bill}}{\text{H}_2\ \text{production rate}}$$

$$= \frac{0.997\ \text{kg} \times 1.035\ \text{W cm}^{-2} \times \$0.02\ \text{kW per h}}{2.59 \times 10^{-6}\ \text{mol H}_2\ \text{per cm}^2\ \text{per s} \times 2\ \text{kg mol}^{-1}}$$

$$= \$1.11/\text{GGE H}_2$$

3. Results and discussion

3.1 Morphological and structural characterization of electrocatalysts

The synthesis method of NFM-LTH/MXene was schematically illustrated in Fig. 1a. Briefly, multi-layered $Ti_3C_2T_x$ MXene was obtained by selective etching of Al from the Ti_3AlC_2 MAX phase with LiF and HCl solution. Following ultrasonic treatment, a few layered exfoliated $Ti_3C_2T_x$ MXene was obtained with many negatively charged functional groups which mainly helps to anchor NFM-LTH nanosheets on $Ti_3C_2T_x$ MXene. After the addition of metal salt solution to the MXene suspension, nucleation starts and *in situ* growth of LTH occurs on the surface of MXene, resulting in the formation of NFM-LTH/MXene hybrid materials. Field emission scanning electron microscopy (FESEM) was used to obtain the morphology of $Ti_3C_2T_x$ MXene, NFM-LTH and NFM-LTH/$Ti_3C_2T_x$ MXene. FESEM images of MXene clearly showed a nanosheet like structure as expected (Fig. S1a†).[26] The corresponding energy dispersive X-ray analysis (EDAX) of $Ti_3C_2T_x$ shows a nominal presence of Al in MXene nanosheets, confirming successful etching of Al metal from bulk MAX phase as depicted in Fig. S1b.† Elemental mapping clearly reflects homogeneous distribution of Ti, C and other elements throughout the nanosheets (Fig. S1c–h†). NFM-LTH was observed as a nanoflake structure that oriented together to form flower-like morphology (Fig. S2a†). The EDAX elemental mapping shows that Ni, Fe and Mo are homogeneously distributed throughout the surface (Fig. S2b–e†). The heterostructure formation combining NFM-LTH and MXene is clearly seen in the FESEM image and TEM image displayed in Fig. 1b and c. The close observation reveals the fact that the flowery nanoflakes of LTHs were grown on MXene nanosheets with largely exposed edges, offering many accessible active sites and openings for easy gas diffusion to favour water electrocatalysis.[35–37] Certainly, the combination of NFM-LTH nanoflakes and MXene nanosheets improve the easy access of electrolyte and provide great conductive support. Such MXene support to NFM-LTH helps to facilitate and shorten the charge transfer pathway, boosting OER mechanism. Further in-depth morphological analysis was carried out by high resolution transmission electron microscopy (HRTEM) and the combination of NFM-LTH and MXene is easily seen in Fig. 1d. The interface of the NFM-LTH/MXene heterostructure is clearly visible, showing characteristic lattice fringes of respective materials with an (012) plane of NiFeMo-LTH and (015) plane of $Ti_3C_2T_x$. Thus, a well-defined interface between LTH and MXene facilitates electron transfer which improves the electrocatalytic activity of the heterostructure. The corresponding SAED pattern in Fig. 1e displays diffused rings for both the materials. This confirms the formation of the NFM-LTH/$Ti_3C_2T_x$ heterostructure, which is believed to be beneficial for rapid electronic charge transfer between two phases. The presence of these two phases and the distribution of their respective elements were investigated using high-angle annular dark-field scanning transmission electron microscopy (HAADF-STEM) and energy dispersive X-ray elemental mapping (Fig. 1f–m and Table S2†). The much-affirmed differences in elemental distribution between the two phases further confirmed the co-existence of NFM-LTH and MXene as intended. The molar ratios of Ni, Fe and Mo in NFM-LTH/MXene and NFM-LTH were 3.28 : 1.35 : 1 and 4.75 : 2.5 : 1, respectively (Table S3†).

The development of MXene, NFM-LTH and NFM-LTH/MXene were further evaluated by XRD analysis (Fig. 2a). The XRD pattern for MXene shows a major peak at 5.94° corresponding to the (002) plane of $Ti_3C_2T_x$, confirming the synthesis of MXene.[38] On the other hand, the formation of NiFeMo-LTH was confirmed from diffraction peaks located at 11.6°, 23.4°, 33.8°, 39.1°, 59.9° and 60.7° corresponding to (003), (006), (012), (015), (110) and (113) planes for LDHs, respectively (JCPDS no. 40-0215).[39] Moving forward, the XRD pattern for NFM-LTH/MXene heterostructure reflects the presence of characteristic peaks for LDH and MXene, confirming the co-existence of the materials. The weakening of (002) peak intensity for MXene was due to the growth of LTHs on the MXene nanosheets. The Raman spectroscopy of MXene, NFM-LTH and NFM-LTH/MXene heterostructures are shown in Fig. S3.† For pristine MXene and heterostructure, the vibrational bands presented at 156 cm^{-1}, 390 cm^{-1}, 599 cm^{-1} can be assigned to the E_g, B_{1g} and A_{1g} modes of $Ti_3C_2T_x$ MXene, respectively.[40] The D (1350 cm^{-1}) and G (1560 cm^{-1}) bands present in MXene and in the heterostructure (with a small shift) is believed to be due to the strong interaction and

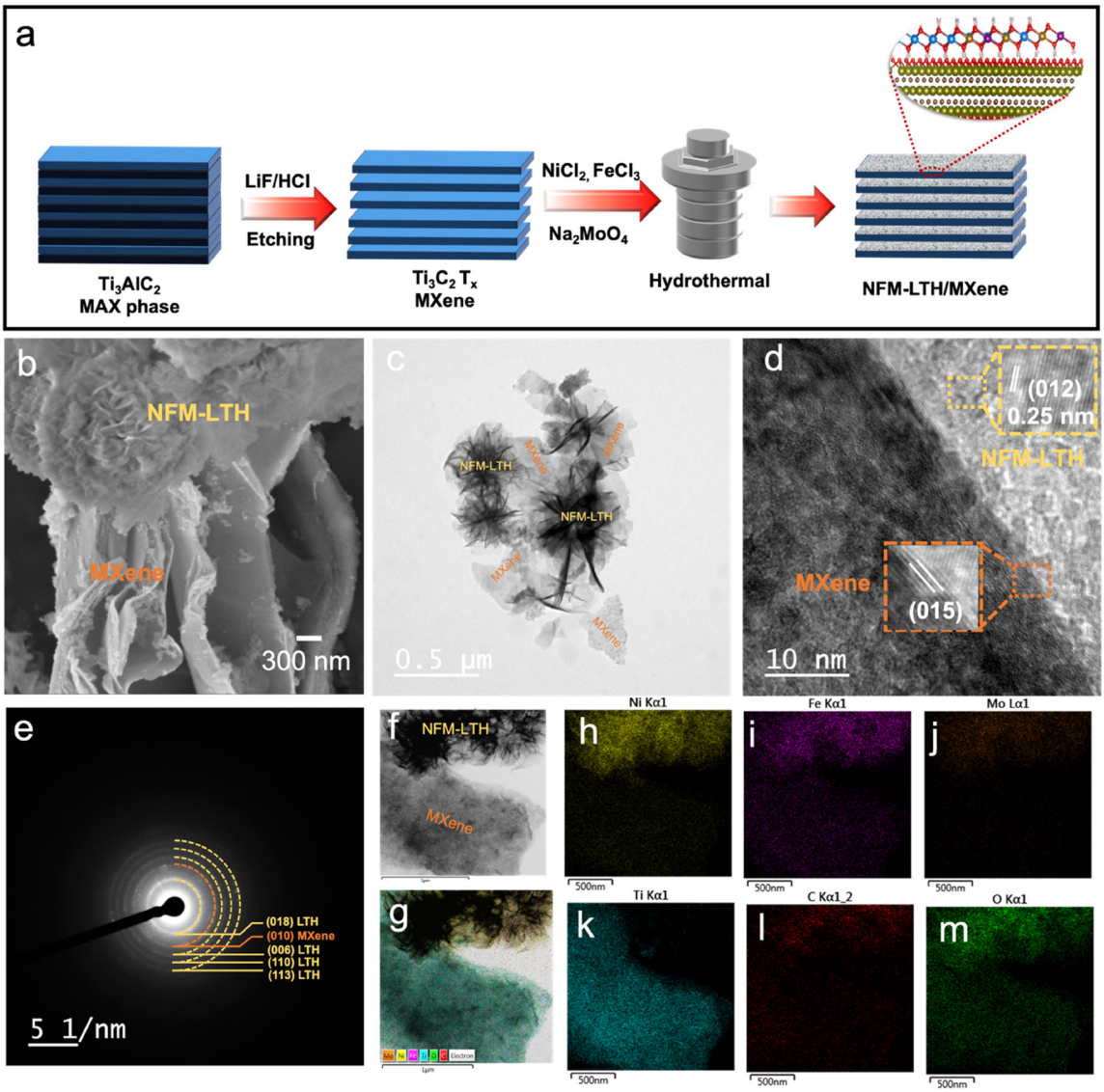

Fig. 1 (a) Schematic of the synthesis of NFM-LTH/MXene. (b) FESEM image, (c) TEM image, and (d) HRTEM image showing clear lattice fringes and (e) SAED pattern of NFM-LTH/MXene. (f–m) HAADF-STEM image and elemental mapping images showing uniform distribution of Ni, Fe, Mo, Ti, C and O elements in distinct LTH and MXene parts in the NFM-LTH/MXene heterostructure.

charge transfer process between LTH and MXene. On the other hand, NFM-LTH shows a broad peak at 250–680 cm^{-1} and around 1000 cm^{-1}, which correspond to the vibration modes of M–O, M–OH and intercalated CO_3^{2-} ions, which are also present in the heterostructure.[21] The surface chemical environment and electronic states of elements present in NFM-LTH/MXene and NFM-LTH were thoroughly examined with the help of X-ray photoelectron spectroscopy (XPS). The XPS spectra confirms the co-existence of Ni, Fe, Mo, O, C, and Ti elements in NFM-LTH/MXene and Ni, Fe, Mo, O, and C in NFM-LTH (Fig. S4†). The high-resolution Ni 2p XPS spectra of NFM-LTH suggests the presence of Ni^{2+} and Ni^{3+} with binding energies of 855.7 eV ($2p_{3/2}$) and 873.3 eV ($2p_{1/2}$), and 857.2 eV ($2p_{3/2}$) and 875.1 eV ($2p_{1/2}$), respectively, along with two satellite peaks (861.6 eV and 878.3 eV), as shown in Fig. 2b.[19] Interestingly, the peak intensity ratio of Ni^{3+}/Ni^{2+} of the NFM-LTH/MXene composite increases from 0.5 to 0.72 (Fig. S5a†), confirming partial oxidation of Ni^{2+} to Ni^{3+}. This phenomenon indicates that MXene is a support material and a driving material for strong electronic communication within LTH and MXene. The development of Ni^{3+} is believed to be beneficial for the OER mechanism as reported elsewhere.[41,42] The core Fe 2p spectra of NFM-LTH shows two distinct doublets of Fe $2p_{3/2}$ and Fe $2p_{1/2}$ at 712.3 eV and 725.4 eV, respectively, combined with two satellite peaks at 717.5 eV and 734.3 eV, respectively (Fig. 2c). Careful deconvolution of the doublets reflects the coexistence of Fe^{2+} and Fe^{3+}.[43] A decrease in peak intensity ratio of Fe^{3+}/Fe^{2+} from 1.75 to 0.83 is noticed in the heterostructure (Fig. S5b†). The high-resolution Mo 3d spectra shows two major peaks at 232.2 eV for Mo $3d_{5/2}$ and at 235.3 eV

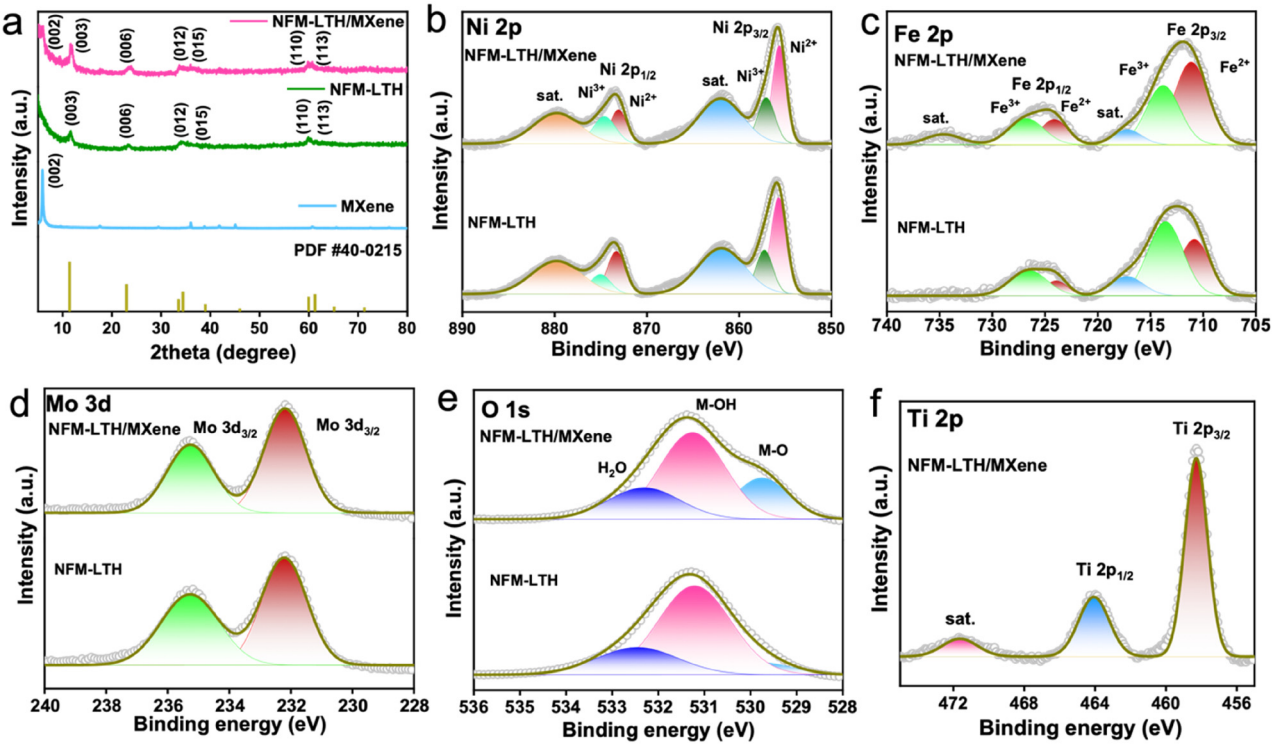

Fig. 2 (a) XRD patterns of NFM-LTH/MXene, NFM-LTH and MXene. (b–f) High resolution XPS spectra of (b) Ni 2p (c) Fe 2p, (d) Mo 3d, (e) O 1s and (f) Ti 2p.

for Mo $3d_{3/2}$, confirming the presence of Mo^{6+} without any significant changes in the NFM-LTH/MXene heterostructure (Fig. 2d). The O 1s spectra shows three distinct peaks located at 529.6 eV, 531.3 eV and 532.5 eV for M–O, M–OH and the absorbed water molecule, respectively (Fig. 2e).[20] Apart from the strong M–OH peak, the stronger M–O peak in the NFM-LTH/MXene heterostructure may be due to the available Ti–O bonds in MXene layers and coordination with metal species of LTH through a bridging oxygen (Fig. S5c†). The Ti 2p spectra in the heterostructure indicates the presence of Ti^{3+} with the characteristic doublets situated at 458.1 and 463.8 eV (Fig. 2f).[29]

3.2 Electrocatalytic activity of NFM-LTH/MXene in 1 M KOH

The electrocatalytic activity of the NFM-LTH/MXene heterostructure towards the OER mechanism was evaluated in 1 M KOH containing freshwater (pH = 13.9) in a three-electrode system and compared with the activities of pristine materials and conventional RuO_2 as a reference. To reduce the influence of capacitive current, the scan rate for the LSV polarization curve was chosen as 2 mV s^{-1}. The LSV polarization plots indicates that the MXene phase is inert towards OER (Fig. 3a), while NFM-LTH is much more active for the OER mechanism. Interestingly, the combination of NFM-LTH and MXene as a heterostructure boosts the OER activity considerably. The activity trend in terms of overpotentials at a current density of 100 mA cm^{-2} was NFM-LTH/MXene (280 mV) < NFM-LTH (330 mV) < RuO_2 (400 mV) < MXene (570 mV) < NF (630 mV). The heterostructure achieved an ultralow overpotential of 220 mV at the benchmark current density of 10 mA cm^{-2} indicates its superiority over other electrocatalysts and the differences in overpotential values at different current densities are represented in a bar diagram (Fig. 3b). In fact, the developed heterostructure outperforms most of the recently reported MXene based electrocatalysts (Fig. 3c and Tables S6, S7†). The elevated current density of NFM-LTH/MXene may be influenced by the high conductivity of nickel foam. To verify this assertion, we checked the OER performances by drop-casting samples on a glassy carbon electrode (GCE) (Fig. S6†). Following the same trend, the heterostructure shows better activity than pristine NFM-LTH with a decrease of 56 mV overpotential at 100 mA cm^{-2} current density. The results demonstrate that MXene helps to improve the activity of NFM-LTH/MXene by providing conductive support driving electronic communication and thereby facilitating the generation of the active site. Moreover, the lower Tafel slope for NFM-LTH/MXene (56 mV dec^{-1}) compared to NFM-LTH (69 mV dec^{-1}), MXene (312 mV dec^{-1}), RuO_2 (262 mV dec^{-1}) and NF (382 mV dec^{-1}) indicates faster OER kinetics of the heterostructure (Fig. 3d). The charge transfer phenomena of developed electrocatalysts were investigated by electrochemical impedance spectroscopy (EIS). The fitted Nyquist plot determines the charge transfer resistance (R_{ct}) values of the electrodes from the radii of semicircles. The lowest R_{ct} value of 0.95 Ω was observed for NFM-LTH/MXene, offering easy charge transfer at the electrode/electrolyte interface compared to pristine NFM-LTH

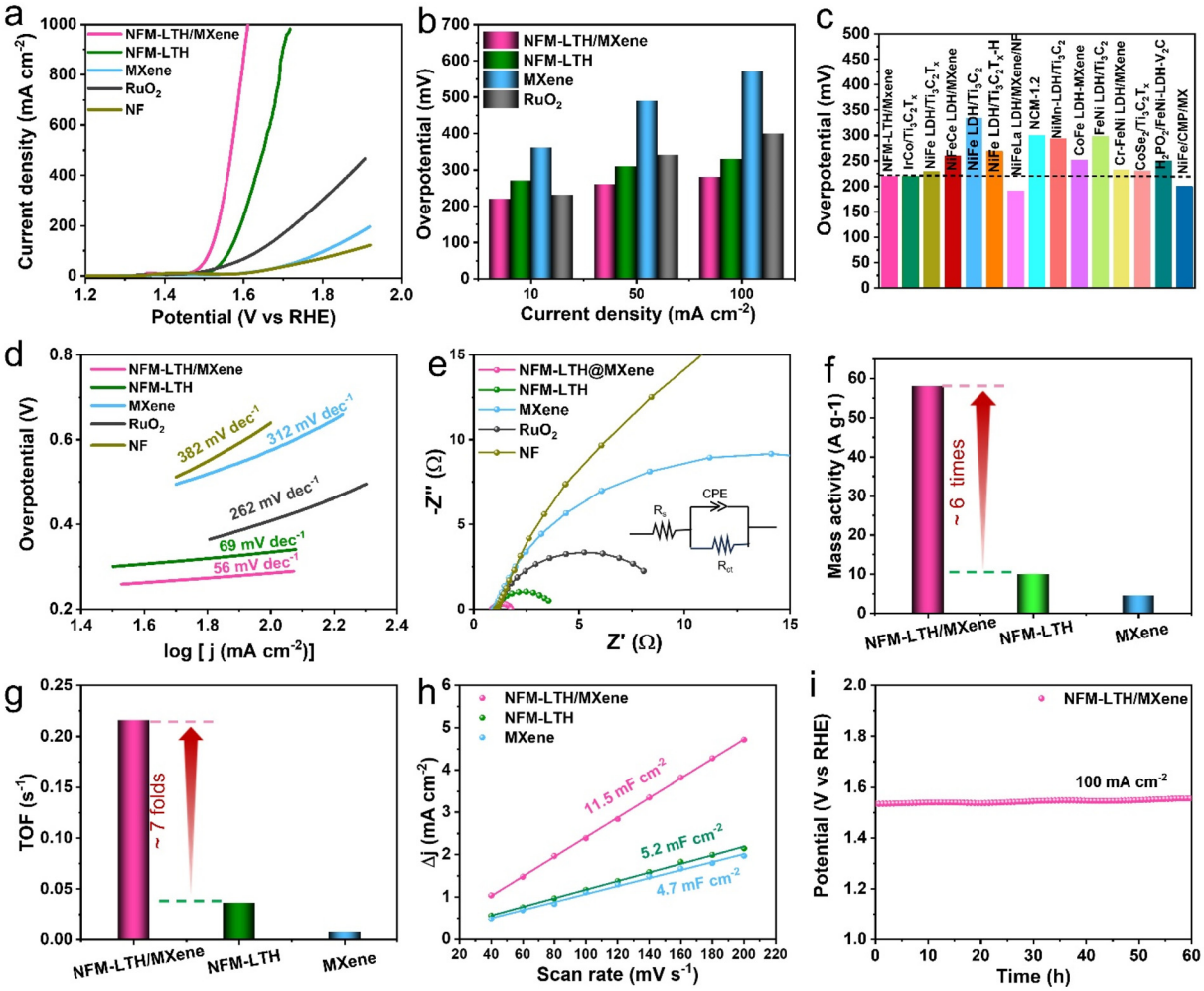

Fig. 3 OER activity in 1 M KOH electrolyte: (a) LSV polarization curves of NFM-LTH/MXene, NFM-LTH, MXene, RuO_2 and NF at a 2 mV s^{-1} scan rate. (b) Comparison of overpotential values at 10, 50 and 100 mA cm^2 current densities for different electrocatalysts. (c) Comparison of the OER overpotential of this work and recently reported MXene based electrocatalysts at a 10 mA cm^{-2} current density. (d) Tafel slope of NFM-LTH/MXene, NFM-LTH, MXene, RuO_2 and NF derived from the LSV curve. (e) Nyquist plots (inset: circuit diagram), (f) mass activity, (g) TOF values and (h) double layer capacitance (C_{dl}) determined for different electrocatalysts. (i) Stability test of NFM-LTH/MXene at 100 mA cm^{-2} current density in 1 M KOH electrolyte medium.

(2.71 Ω) and MXene (19.9 Ω) (Fig. 3e and Table S4†). The lower R_{ct} of the heterostructure was due to the presence of the edge exposed LTH nanoflakes, which provides a shorter electron pathway that hastens charge transfer at electrode–electrolyte interface. Thus, it is believed that the presence of MXene acts as a conductive support material and facilitates the electron transfer between LTH and MXene as evidenced from XPS analysis, resulting in higher OER activity for the NFM-LTH/MXene heterostructure. Mass activity is an important parameter to evaluate the electrochemical activities of electrocatalysts. The NFM-LTH/MXene heterostructure exhibited higher mass activity of 58 A g^{-1} at an overpotential of 250 mV compared to the others (Fig. 3f), implying the capability of fast mass transfer facilitating the OER mechanism. In fact, the mass activity was boosted by almost six times compared to pristine NFM-LTH, suggesting significant improvisation towards OER activity due to the synergistic effect between LTH and MXene. Moreover, the morphology of the heterostructure plays a big role as LTH nanoflakes on MXene nanosheets reduce the mass diffusion and prevent bubble accumulation during the OER, hastening the process. The intrinsic activity of electrocatalysts were also evaluated by determining the turn over frequency (TOF, s^{-1}) obtained from the redox active area calculation at 250 mV overpotential (Fig. S7†). As anticipated, the NFM-LTH/MXene poses the highest TOF value among all the prepared electrocatalysts, and is seven-fold higher than NFM-LTH (Fig. 3g). The determination of the electrochemical active surface area (ECSA) is considered to reflect the real electroactive sites, which linearly varies with the double-layer capacitance (C_{dl}) values evaluated by measuring CVs at different scan rates from a non-faradaic region (Fig. S8a–c†). In line with other inherent electrochemical properties, the heterostructure

exhibited the highest C_{dl} value of 11.5 mF cm^{-2}, which is two times higher than NFM-LTH (Fig. 3h). The high ECSA or C_{dl} values of the heterostructure (Fig. S8d†) suggests that the MXene nanosheets support NFM-LTH and facilitate the easy penetration of alkaline electrolyte to the active sites of LTH nanoflakes, increasing the availability of catalytically exposed active sites during OER compared with other electrocatalysts. The results support the superior OER performance of NFM-LTH/MXene compared to the other structures (Table S5†). The robustness of NFM-LTH/MXene was checked by performing stability tests at constant current density. The electrocatalyst shows a steady potential at fixed current density of 100 mA cm^{-2} for more than 60 h in 1 M KOH, confirming its great stability (Fig. 3i). Importantly, the performance in terms of the LSV plot remains unchanged after such long operation, as shown in Fig. S9.†

3.3 Electrolyzer performance of NFM-LTH/MXene

Following the excellent OER activity and robust stability of NFM-LTH/MXene heterostructure in alkaline medium, we further explored its performance in an anion exchange membrane alkaline water electrolyzer (AEMWE) set up. The AEMWE set up was assembled by combining NFM-LTH/MXene on NF as the anode, commercial Pt/C on Ni foam as the cathode and Sustainion membrane between the anode and cathode (Fig. 4a). The digital image of the electrolyzer is shown in Fig. 4b. The influence of the developed heterostructure is clearly shown as the electrolyzer only needs 2.16 V to attain an industry level current density of 0.75 A cm^{-2}, which is almost 2.5 times more efficient than the commercial RuO_2||Pt/C based electrolyzer at 60 °C (Fig. 4c). This saves a considerable amount of energy, making the electrolyzer efficient enough. The economic efficiency of electrolyzer is an important factor its commercialization. It was calculated to be 60.5%, which is acceptable for practical consideration.[33] Further, the corresponding energy consumption and price per gasoline-gallon equivalent (GGE) H_2 were estimated to be 55.5 kW h and US $1.11 which is almost half of the target cost (US$2.00) for H_2 production in 2026 as directed by Department of Energy, USA.[44] Further, to evaluate its durability, a chronopotentiometry was performed study at current densities of 100 and 200 mA cm^{-2}, showcasing robust stability over 30 h of electrolysis (Fig. 4d). Further, an H_2 production rate of 4.5 ml min^{-1} was achieved by collecting H_2 and O_2 gases at different time intervals upon applied current density of 100 mA cm^{-2} (Fig. 4e). Thereby, after over 30 h of operation a total amount of about 8 L H_2 was produced, which may further improve towards large scale hydrogen production upon scalability of the technology in near future. For better clarity, a comprehensive assessment has been tabulated in Table S8† by comparing our electrolyzer performance with other reported state-of-the-art electrolyzers. Notably, our electrolyzer was quite impressive in terms of activity, durability, hydrogen production rate, performance and economic efficiency.

3.4 Electrochemical activity in alkaline highly saline, simulated seawater and real seawater media

After showcasing the impressive activity in 1 M KOH containing freshwater, NFM-LTH/MXene heterostructure was further explored in alkaline saline water (1 M KOH + 0.5 M NaCl),

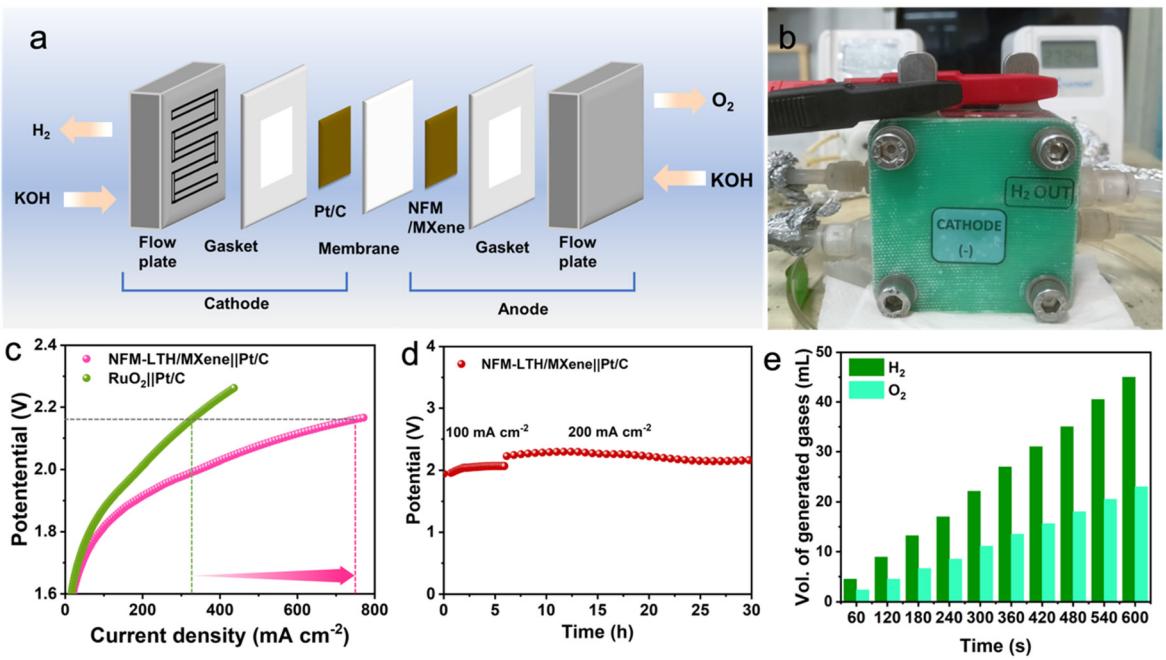

Fig. 4 AEM water electrolyzer performance in 1 M KOH medium. (a) Schematic of AEMWE components. (b) Digital image of AEMWE. (c) Polarization plots of NFM-LTH/MXene||Pt/C *vs.* RuO_2||Pt/C taken at a 60 °C operating temperature. (d) Chronopotentiometry test of the electrolyzer performed at an applied current density of 100 and 200 mA cm^{-2}. (e) H_2 and O_2 gases collected at different time intervals.

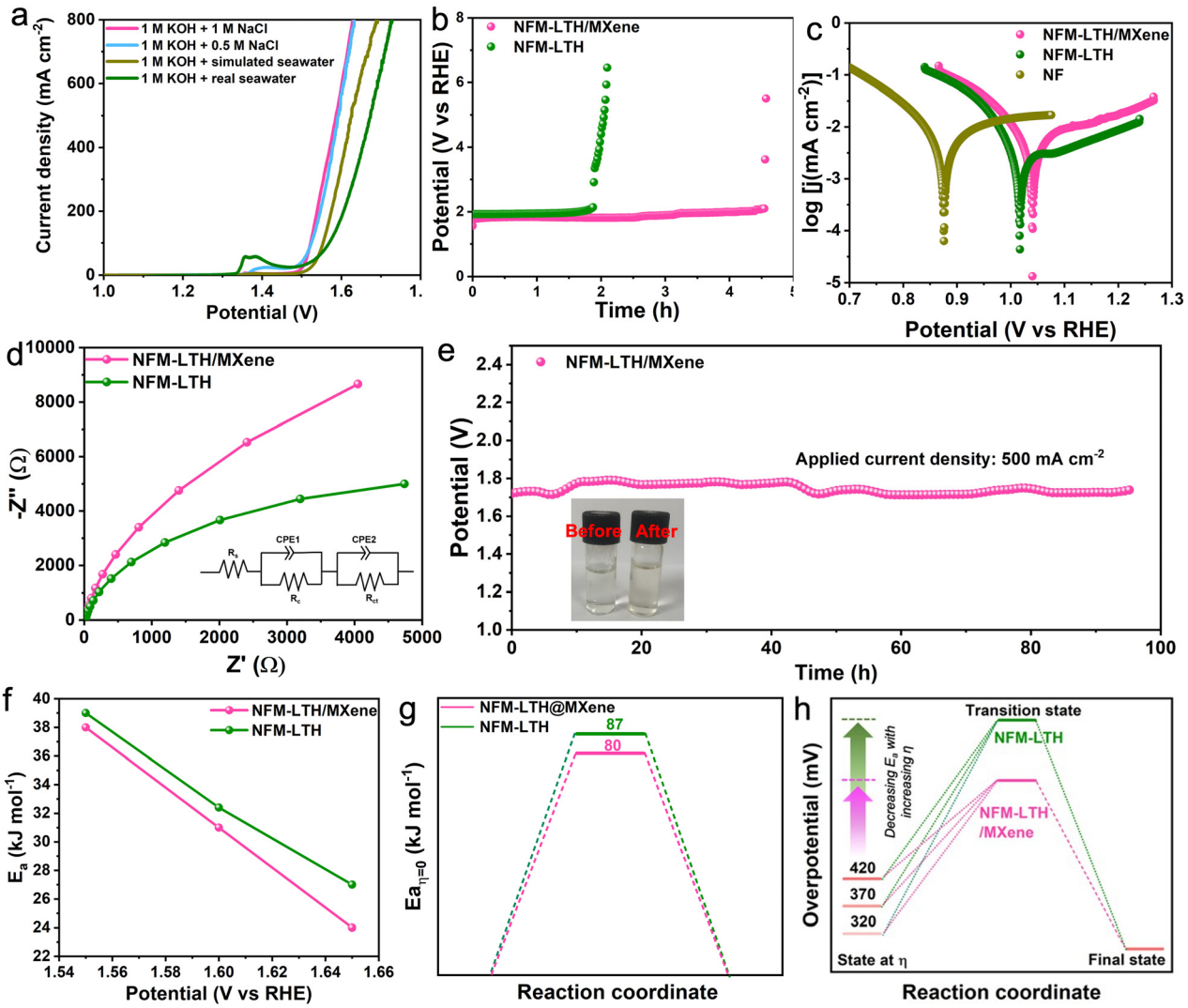

Fig. 5 OER performance evaluation in saline- and seawater-based electrolytes. (a) LSV polarization curves of NFM-LTH/MXene taken at a 2 mV s^{-1} scan rate in different electrolyte medium. (b) Chronopotentiometry study of NFM-LTH/MXene and NFM-LTH at a current density of 1 A cm^{-2} in highly saline alkaline electrolyte. (c) Potentiodynamic polarization curves for NFM-LTH/MXene, NFM-LTH and NF and (d) Nyquist plot (inset: fitted circuit) taken at OCP for NFM-LTH/MXene and NFM-LTH in 1 M KOH + 1 M NaCl electrolyte. (e) Chronopotentiometry test at an operating current density of 500 mA cm^{-2} in real alkaline seawater electrolyte (inset: iodometry test). (f) Activation energy (E_a) variation at different oxidation potentials, (g) E_a obtained at equilibrium state and (h) reaction paths in terms of overpotential along the reaction coordinate for NFM-LTH/MXene and NFM-LTH in alkaline real seawater electrolyte.

highly saline water (1 M KOH + 0.5 M NaCl), alkaline simulated seawater and real seawater medium. The LSV polarization curves show outstanding activity of NFM-LTH/MXene with η_{100} of 292 mV, 295 mV, 322 mV and 340 mV in 1 M KOH + 1 M NaCl, 1 M KOH + 0.5 M NaCl, alkaline simulated and real seawater, respectively (Fig. 5a). Meanwhile, the activities are much more comparable in saline water in simulated and real seawater, irrespective of NaCl concentration. The activity is compromised to some extent due to the presence of various elements. Importantly, the catalyst achieved a 500 mA cm^{-2} current density at 354 mV, 362 mV, 397 mV and 440 mV in 1 M KOH + 1 M NaCl, 1 M KOH + 0.5 M NaCl, 1 M KOH + simulated seawater and 1 M KOH + real seawater electrolytes, respectively which is well below the CER limiting potential of 480 mV. The charge transfer resistance values from Nyquist plots were 1.1 Ω and 1.24 Ω in saline and real seawater, respectively, indicating efficient charge transfer at the electrode–electrolyte interface (Fig. S10†). Considering durability as the major concern for seawater electrolysis owing to the presence of corrosive chloride ions, we examined the ability of the NFM-LTH/MXene heterostructure and compared it with pristine NFM-LTH through a chronopotentiometry study at a high applied current density of 1 A cm^{-2} in highly saline media (Fig. 5b). Interestingly, NFM-LTH/MXene exhibited much longer stability of 4.5 h than pristine NFM-LTH (1.9 h), even though the potentials were beyond 1.72 V. This indicates that NFM-LTH/MXene has greater sustainability along with good activity compared to its LTH counterpart in harsh con-

ditions with double the chloride concentration than that in real seawater. We further examined the stability of NFM-LTH/MXene in different comparable salt concentrations like seawater, for example, in 1 M KOH + 0.5 M NaCl and 1 M KOH + simulated seawater in high current densities of 1 and 0.5 A cm^{-2}, as shown in Fig. S11.† Impressively, an outstanding stability was achieved for over 120 h in 1 M KOH + 0.5 M NaCl and about 80 h in alkaline simulated seawater, reflecting its great ability to restrict chloride corrosion. The corrosion polarization plots for NFM-LTH/MXene, NFM-LTH and NF in 1 M KOH + 1 M NaCl were compared to explore the corrosion resistant ability of LTH/MXene heterostructures (Fig. 5c). The superior corrosion resistance ability for LTH/MXene was confirmed from the more positive corrosion potential (E_{corr}, 1.04 V) and lower corrosion current density (I_{corr}, 1.28×10^{-5} A cm^{-2}) compared with pristine NFM-LTH (1.01 V and 4.07×10^{-5} A cm^{-2}) and NF (0.87 V and 6.30×10^{-5} A cm^{-2}) (Table S9†). Besides, the EIS study at OCP was performed to determine different corrosion parameters of the anode, including solution resistance (R_s), corrosion resistance (R_c) and charge transfer resistance (R_{ct}) (Fig. 5d and Table S10†). The higher R_c and R_{ct} values of NFM-LTH/MXene compared with NFM-LTH confirms its better corrosion resistance ability than NFM-LTH.[45,46] Owing to such great ability, the stability of NFM-LTH/MXene in real alkaline seawater electrolyte was examined at a constant current density of 500 mA cm^{-2}. Impressively, the NFM-LTH/MXene electrocatalyst exhibited a steady performance over more than 95 h without any noticeable change distinguishing the effect of MXene towards protecting electrode from chloride corrosion (Fig. 5e). The possible formation of ClO^- during the seawater electrolysis was further examined with the help of the iodometry test. The near lack of yellow coloration of the electrolyte sample after long hours of stability tests ruled out chloride corrosion (inset: Fig. 5e). Only a handful of literature has revealed such corrosion resistance behaviour of MXene, and to the best of our knowledge, this is the first report on its application in sustainable seawater oxidation.[47,48]

To evaluate the synergistic effect of MXene and LTH upon the kinetic behaviour of electrocatalysts towards seawater oxidation, activation energies (E_a) of NFM-LTH/MXene and pristine NFM-LTH were evaluated with the help of the temperature dependent Arrhenius equation:[49,50]

$$\ln j = -\frac{E_a}{RT} + C \quad (8)$$

where j is the current density, E_a is the activation energy, T is the absolute temperature (K) and R is the universal gas constant. The temperature dependent LSV polarization curves are shown in Fig. S12a and b† and the slope of $\log j$ *vs.* $1000/T$ displayed in Fig. S12c and d† was used to determine the activation energies (E_a) of electrocatalysts at different oxidation potentials. Linearity was well-maintained in the $\log j$ *vs.* $1000/T$ plot (Arrhenius plot) in both cases, suggesting the interfacial charge transfer as the rate-determining step (RDS). The plotted E_a at different potentials depicts the fact that the NFM-LTH/MXene heterostructure has lower activation energy than NFM-LTH (Fig. 5f). The linear plot was extrapolated to zero overpotential ($\eta = 0$) to acquire information about the kinetic energy barrier at equilibrium. The obtained values of $E_a^{\eta=0}$ corresponding to NFM-LTH/MXene and NFM-LTH are 80 and 87 kJ mol^{-1}, respectively (Fig. 5g). This suggests that the lower $E_a^{\eta=0}$ for the heterostructure supports faster kinetics towards OER with the LTH/MXene combination. To understand the relationship between E_a and η in a better way, the reaction pathway are represented in in terms of different overpotentials for both electrocatalysts (Fig. 5h). The activation energy decreases with increasing η. Likewise, the overpotential value at zero activation energy ($\eta^{E_a=0}$) indicates the energy required to overcome the kinetic energy barrier for the OER.[49] As expected, the LTH/MXene heterostructure requires much lower potential to overcome kinetic energy barrier for the OER, making the combination superior in alkaline seawater than the pristine LTH.

3.5 Post OER characterization and proposed mechanism

The robustness of NFM-LTH/MXene after prolonged seawater oxidation was evaluated by FESEM, XPS and Raman spectroscopy analysis. The FESEM image confirms the existence of MXene sheets and LTH nanoflakes (Fig. S13a and b†) along with homogeneous distribution of Ni, Fe, Mo, Ti, C and O elements throughout the material even after 100 h of continuous seawater oxidation, which demonstrates the robustness of the heterostructure, as shown by EDAX elemental mapping (Fig. S13c–h†). Raman spectroscopy was used to explore the surface alteration of NFM-LTH/MXene under different oxidation potentials in such harsh condition (Fig. 6a). At the OCP condition, the Raman bands at 470 cm^{-1} and 575 cm^{-1} are identified as the stretching vibration mode of Ni^{II}–O for $Ni(OH)_2$[51] while bands at 305 cm^{-1} and 680 cm^{-1} correspond to weak vibration of Fe^{III}–O in NiFe hydroxides.[52] At an anodic potential of 1.4 V, the development of a broad band in the range of 500–600 cm^{-1} can be noticed, indicating partial oxidation at an anode surface which transforms into two distinct Raman peaks at 480 cm^{-1} and 560 cm^{-1} at higher anodic potential (1.6 V and onwards).[53] These characteristic bands correspond to the E_g and A_{1g} vibration modes of Ni^{III}–O for NiOOH due to surface reconstruction during seawater oxidation, often recognized as an active site beneficial for water oxidation.[49,54] The bands remain prominent without the appearance of any new bands after prolonged operation (100 h), confirming the robustness of the electrocatalyst. On the contrary, the bands corresponding to Fe–O are suppressed compared to intensified Ni^{III}–O bands and remain as weak bands, suggesting that NiOOH acts as the active site during OER, not FeOOH. Besides a broad band is observed in the range of 900–1100 cm^{-1} at higher anodic potential, supporting the formation of NiOO-species.[55,56] The observation was further assessed by XPS analysis (Fig. 6b–f). As expected, the main peak of Ni 2p was shifted by 0.16 eV towards higher binding energy (Fig. 6b) at higher oxidation potentials and a gradual

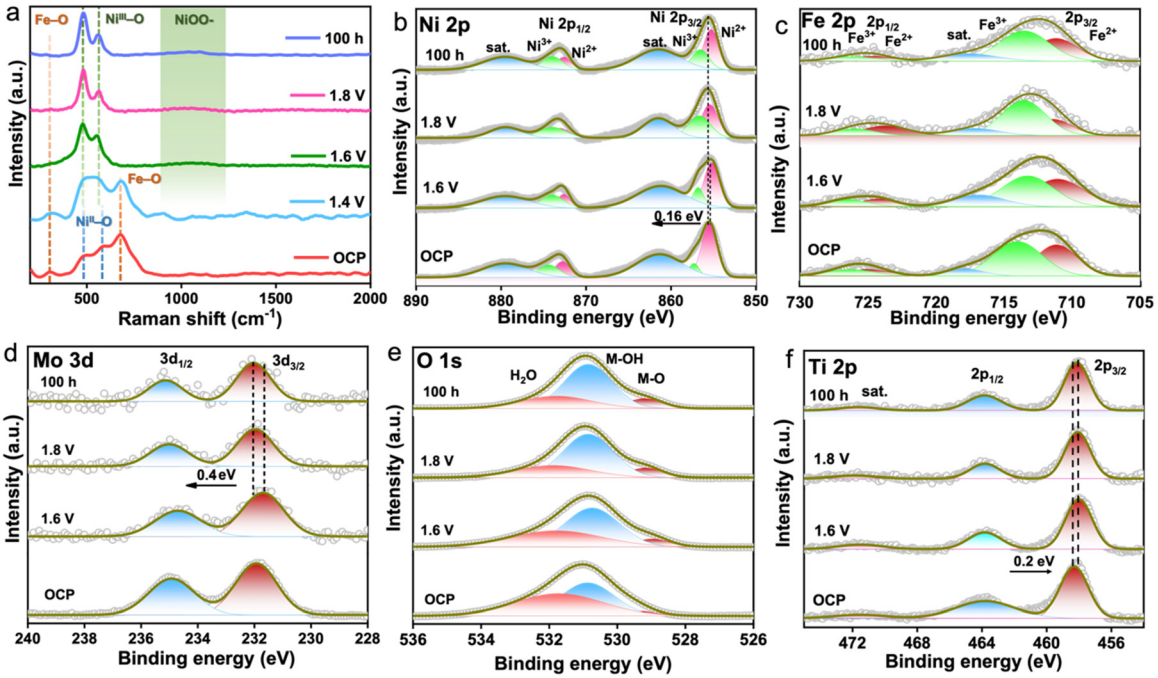

Fig. 6 (a) Raman spectroscopy and (b–f) XPS spectra of NFM-LTH/MXene for each element at different oxidation potentials and after 100 h of operation in 1 M KOH + real seawater electrolyte.

increase of Ni^{3+}/Ni^{2+} ratio can be seen (Fig. S14†). This observation supports partial oxidation of Ni^{2+} to Ni^{3+} and the formation of NiOOH is also seen in Raman analysis.[57,58] In line with Raman analysis, the Fe^{3+}/Fe^{2+} ratio decreases upon applied anodic potential compared to the OCP condition, ruling out Fe oxidation (Fig. 6c and Fig. S14†). Further, the shift of Mo 3d towards higher binding energy was observed due to long exposure in oxidative conditions (Fig. 6d), which facilitates the stabilization of electroactive species during OER.

Besides, the peak intensity of M–OH increases with greater potential and 100 h exposure, reflecting the formation of oxyhydroxide species during water oxidation (Fig. 6e).[59] On the other hand, a negative shift by 0.2 eV for Ti 2p (Fig. 6f) is possibly due to partial reduction of Ti^{3+} to Ti^{2+}, stabilizing the oxidized species (Ni^{3+}) in LTH, which helps boost the OER activity. The transfer of electrons from LTH to MXene is probably due to the presence of a vacant d-orbital in Ti^{3+} (d^1), which can easily accommodate electrons from Ni^{2+} in LTH. Besides, the presence of terminal functional groups (–OH, –F, –O) in MXene helps to strongly coordinate with LTH, allowing facile electron transportation through Ni–O–Ti pathway.[60] Therefore, the evidences confirm the fact that MXene not only act as ESI,† but also takes part in strong electronic interaction between the metal species within LTH and MXene, as illustrated in Fig. 7. In a way, MXene is believed to indirectly participate by activating LTH favouring OER activity. This clearly supports the boosted OER activity of LTH/MXene heterostructure compared to active LTH and relatively inactive pristine MXene.

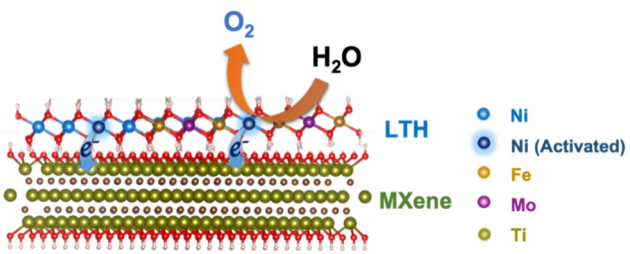

Fig. 7 Schematic of electronic communication between LTH and MXene, which is responsible for the boosted OER performance.

Moreover, the anti-corrosive ability of MXene adds to the robustness of the electrocatalyst, allowing sustainable seawater oxidation over long hours.

4. Conclusions

We have fabricated a heterostructure by combining a NiFeMo layered triple hydroxide on $Ti_3C_2T_x$ MXene using a simple hydrothermal method. The heterostructure leads to superior OER activity with an overpotential of 220 V at 10 mA cm^{-2} current density and good stability over 60 h in alkaline freshwater. The impressive OER activity of the heterostructure is due to the strong electronic coupling between two phases and formation of electroactive sites. Further, the combination of NiFeMn-LTH/MXene||Pt/C in the electrolyzer cell set up of AEMWE conveyed the impressive improvement in the activity, durability, hydrogen production rate and economic efficiency

of water splitting to produce hydrogen compared to conventional RuO_2‖Pt/C. The combination in AEMWE achieved an industrial level current density of 750 mA cm^{-2} at 2.16 V cell voltage, maintained a steady operation over 30 h and displayed good electrolyzer efficiency of 60.5%. The estimated H_2 production cost per GGE was only $1.11, which is well below to the targeted value by the DoE, USA, indicating that it can be implemented as a potential performer for industry. The electrocatalysts were also implemented for seawater oxidation and found to be active and stable without generating hypochlorite species during 100 h operation. The lowering of the activation energy of NiFeMn-LTH/MXene compared with NiFeMn-LTH is an important factor for boosting OER kinetics. The post OER stability characterization of anode confirms the formation of NiOOH as the main active species that maintains the OER activity and stability. In fact, MXene in the heterostructure acted as a conductive support material, indirectly facilitated activation by easy electronic transportation from LTH to MXene, generating electroactive species in favour of the OER, and imparted a corrosion resistive ability, making the electrocatalyst robust enough for seawater oxidation.

Data availability

The data supporting this article have been included as part of the ESI.†

Conflicts of interest

There are no conflicts to declare.

Acknowledgements

P. R. gratefully acknowledges the financial support from the Anusandhan National Research Foundation (ANRF) under the SERB-POWER scheme (SPG/2021/002612) for this work. E. C. would like to thank CSIR-Central Mechanical Engineering Research Institute (CMERI) for in-house project OLP244612 for the MXene related part of this work.

References

1 M. S. Dresselhaus and I. L. Thomas, *Nature*, 2001, **414**, 332–337.
2 J. Goldemberg, *Science*, 2007, **315**, 808–810.
3 A. Sartbaeva, V. L. Kuznetsov, S. A. Wells and P. P. Edwards, *Energy Environ. Sci.*, 2008, **1**, 79.
4 J. A. Turner, *Science*, 2004, **305**, 972–974.
5 F. Song, L. Bai, A. Moysiadou, S. Lee, C. Hu, L. Liardet and X. Hu, *J. Am. Chem. Soc.*, 2018, **140**, 7748–7759.
6 S. Li, E. Li, X. An, X. Hao, Z. Jiang and G. Guan, *Nanoscale*, 2021, **13**, 12788–12817.
7 Y. Bao, X. Liang, H. Zhang, X. Bu, Z. Cai, Y. Yang, D. Yin, Y. Zhang, L. Chen, C. Yang, X. Hu, X. C. Zeng, J. C. Ho and X. Wang, *Adv. Energy Mater.*, 2024, **14**, 2401909.
8 Y. Hu, T. Shen, Z. Wu, Z. Song, X. Sun, S. Hu and Y. Song, *Adv. Funct. Mater.*, 2025, **35**, 2413533.
9 S. Dresp, F. Dionigi, M. Klingenhof and P. Strasser, *ACS Energy Lett.*, 2019, **4**, 933–942.
10 E. Enkhtuvshin, S. Yeo, H. Choi, K. M. Kim, B. An, S. Biswas, Y. Lee, A. K. Nayak, J. U. Jang, K. Na, W. Choi, G. Ali, K. H. Chae, M. Akbar, K. Y. Chung, K. Yoo, Y. Chung, T. H. Shin, H. Kim, C. Chung and H. Han, *Adv. Funct. Mater.*, 2023, **33**, 2214069.
11 W. Tong, M. Forster, F. Dionigi, S. Dresp, R. Sadeghi Erami, P. Strasser, A. J. Cowan and P. Farràs, *Nat. Energy*, 2020, **5**, 367–377.
12 F. Dionigi, T. Reier, Z. Pawolek, M. Gliech and P. Strasser, *ChemSusChem*, 2016, **9**, 962–972.
13 S. Khatun, H. Hirani and P. Roy, *J. Mater. Chem. A*, 2021, **9**, 74–86.
14 S. Guo and S. C. Tan, *Joule*, 2024, **8**, 291–294.
15 C. Ge, S. Guo, W. Li, X. Zhang, B. Chen, X. Feng, S. Yang, D. Xu, Z. Yu, S. K. Ravi, W. Xu, J. Fang and S. C. Tan, *Adv. Funct. Mater.*, 2025, 2421067.
16 J. G. Vos, T. A. Wezendonk, A. W. Jeremiasse and M. T. M. Koper, *J. Am. Chem. Soc.*, 2018, **140**, 10270–10281.
17 C. Das and P. Roy, *Chem. Commun.*, 2022, **58**, 6761–6764.
18 S. Pal, K. Shimizu, S. Khatun, S. Singha, S. Watanabe and P. Roy, *J. Mater. Chem. A*, 2023, **11**, 12151–12163.
19 S. Pal, S. Khatun and P. Roy, *Mater. Adv.*, 2024, **5**, 5156–5166.
20 S. Khatun and P. Roy, *Chem. Commun.*, 2022, **58**, 1104–1107.
21 S. Khatun and P. Roy, *ACS Appl. Energy Mater.*, 2024, **7**, 9110–9120.
22 S. Dresp, T. N. Thanh, M. Klingenhof, S. Brückner, P. Hauke and P. Strasser, *Energy Environ. Sci.*, 2020, **13**, 1725–1729.
23 D. Tyndall, M. J. Craig, L. Gannon, C. McGuinness, N. McEvoy, A. Roy, M. García-Melchor, M. P. Browne and V. Nicolosi, *J. Mater. Chem. A*, 2023, **11**, 4067–4077.
24 D. Wang, L. Liu, Y. Liu, W. Luo, Y. Xie, T. Xiao, Y. Wang, Z. Song, H. Zhang and X. Wang, *ACS Sustainable Chem. Eng.*, 2023, **11**, 16479–16490.
25 M. Naguib, V. N. Mochalin, M. W. Barsoum and Y. Gogotsi, *Adv. Mater.*, 2014, **26**, 992–1005.
26 B. Anasori, M. R. Lukatskaya and Y. Gogotsi, *Nat. Rev. Mater.*, 2017, **2**, 16098.
27 J. Sheng, J. Kang, P. Jiang, K. Meinander, X. Hong, H. Jiang, Nonappa, O. Ikkala, H. Komsa, B. Peng and Z. Lv, *Small*, 2025, **21**, 2404927.
28 C. Shang, D. Sang, C. Li, L. Zou, J. Wu and Q. Wang, *APL Mater.*, 2024, **12**, 060601.
29 M. Yu, Z. Wang, J. Liu, F. Sun, P. Yang and J. Qiu, *Nano Energy*, 2019, **63**, 103880.
30 Y. Chen, H. Yao, F. Kong, H. Tian, G. Meng, S. Wang, X. Mao, X. Cui, X. Hou and J. Shi, *Appl. Catal., B*, 2021, **297**, 120474.
31 L. Hu, R. Xiao, X. Wang, X. Wang, C. Wang, J. Wen, W. Gu and C. Zhu, *Appl. Catal., B*, 2021, **298**, 120599.

32 L. Yan, Z. Du, X. Lai, J. Lan, X. Liu, J. Liao, Y. Feng and H. Li, *Int. J. Hydrogen Energy*, 2023, **48**, 1892–1903.
33 X. Kang, F. Yang, Z. Zhang, H. Liu, S. Ge, S. Hu, S. Li, Y. Luo, Q. Yu, Z. Liu, Q. Wang, W. Ren, C. Sun, H. M. Cheng and B. Liu, *Nat. Commun.*, 2023, **14**, 3607.
34 Y. Chen, Q. Li, Y. Lin, J. Liu, J. Pan, J. Hu and X. Xu, *Nat. Commun.*, 2024, **15**, 7278.
35 C. Wang, Q. Zhang, Z. Liu, B. Li, W. Zhao, C. Zhang, S. Jiang, J. Wang, K. Liu and S. He, *ChemSusChem*, 2024, **17**, e202301703.
36 C. Wang, Q. Zhang, B. Li, Z. Liu, C. He, G. Yang, L. Jiang, C. Zhang, K. Liu and S. He, *Colloids Surf., A*, 2024, **684**, 133228.
37 B. Li, S. Fei, Z. Liu, C. Wang, Z. Sun, C. Zhang, H. Yang, H. Zhao, Q. Zhang and S. He, *Green Chem.*, 2025, **27**, 3099–3107.
38 M. Yu, J. Zheng and M. J. Guo, *Energy Chem.*, 2022, **70**, 472–479.
39 J. Qu, F. Li, M. X. Wang, S. Subakti, M. Deconinck, G. Chen, Y. Li, L. Liu, X. Wang, M. Yu, D. Wolf, A. Lubk, B. Büchner, Y. Vaynzof, O. G. Schmidt and F. Zhu, *Adv. Mater. Interfaces*, 2022, **9**, 2200973.
40 M. Naguib, O. Mashtalir, M. R. Lukatskaya, B. Dyatkin, C. Zhang, V. Presser, Y. Gogotsi and M. W. Barsoum, *Chem. Commun.*, 2014, **50**, 7420–7423.
41 Y. Wang, S. Tao, H. Lin, S. Han, W. Zhong, Y. Xie, J. Hu and S. Yang, *RSC Adv.*, 2020, **10**, 33475–33482.
42 Z. Xu, Y. Ying, G. Zhang, K. Li, Y. Liu, N. Fu, X. Guo, F. Yu and H. Huang, *J. Mater. Chem. A*, 2020, **8**, 26130–26138.
43 X. Meng, J. Han, L. Lu, G. Qiu, Z. L. Wang and C. Sun, *Small*, 2019, **15**, 1902551.
44 U.S. Department of Energy, U.S. National Clean Hydrogen Strategy and Roadmap, 2022.
45 T. Chen, H. John, J. Xu, Q. Lu, J. Hawk and X. Liu, *Corros. Sci.*, 2013, **77**, 230–245.
46 B. G. Prakashaiah, D. V. Kumara, A. A. Pandith, A. N. Shetty and B. E. A. Rani, *Corros. Sci.*, 2018, **136**, 326–338.
47 F. Sun, J. Qin, Z. Wang, M. Yu, X. Wu, X. Sun and J. Qiu, *Nat. Commun.*, 2021, **12**, 4182.
48 X. Wu, S. Zhou, Z. Wang, J. Liu, W. Pei, P. Yang, J. Zhao and J. Qiu, *Adv. Energy Mater.*, 2019, **9**, 1901333.
49 Z. Lin, P. Bu, Y. Xiao, Q. Gao and P. Diao, *J. Mater. Chem. A*, 2022, **10**, 20847–20855.
50 T. A. Zegeye, W.-T. Chen, C.-C. Hsu, J. A. A. Valinton and C.-H. Chen, *ACS Energy Lett.*, 2022, **7**, 2236–2243.
51 Y. Kuang, M. J. Kenney, Y. Meng, W.-H. Hung, Y. Liu, J. E. Huang, R. Prasanna, P. Li, Y. Li, L. Wang, M.-C. Lin, M. D. McGehee, X. Sun and H. Dai, *Proc. Natl. Acad. Sci. U. S. A.*, 2019, **116**, 6624–6629.
52 Y. Wu, J. Yang, T. Tu, W. Li, P. Zhang, Y. Zhou, J. Li, J. Li and S. Sun, *Angew. Chem., Int. Ed.*, 2021, **60**, 26829–26836.
53 Z. Xu, Q. Chen, Q. Chen, P. Wang, J. Wang, C. Guo, X. Qiu, X. Han and J. Hao, *J. Mater. Chem. A*, 2022, **10**, 24137–24146.
54 H. Wang, Y. Hsu, R. Chen, T. Chan, H. M. Chen and B. Liu, *Adv. Energy Mater.*, 2015, **5**, 1500091.
55 S. Zuo, Z. Wu, H. Zhang and X. W. Lou, *Adv. Energy Mater.*, 2022, **12**, 2103383.
56 K. M. Cole, D. W. Kirk and S. J. Thorpe, *J. Electrochem. Soc.*, 2018, **165**, J3122–J3129.
57 H. Lei, L. Ma, Q. Wan, S. Tan, B. Yang, Z. Wang, W. Mai and H. J. Fan, *Adv. Energy Mater.*, 2022, **12**, 2202522.
58 Y. Ding, Z. Wang, Z. Liang, X. Sun, Z. Sun, Y. Zhao, J. Liu, C. Wang, Z. Zeng, L. Fu, M. Zeng and L. Tang, *Adv. Mater.*, 2023, 2302860.
59 I. Chauhan, K. K. Patra, H. Bajpai, N. B. Mhamane, K. N. Salgaonkar and C. S. Gopinath, *Dalton Trans.*, 2023, **52**, 2051–2061.
60 M. Yu, S. Zhou, Z. Wang, J. Zhao and J. Qiu, *Nano Energy*, 2018, **44**, 181–190.